

## Interfacial magnetic coupling between Fe nanoparticles in Fe–Ag granular alloys

This article has been downloaded from IOPscience. Please scroll down to see the full text article.

2012 Nanotechnology 23 025705

(<http://iopscience.iop.org/0957-4484/23/2/025705>)

View [the table of contents for this issue](#), or go to the [journal homepage](#) for more

Download details:

IP Address: 164.54.85.163

The article was downloaded on 15/12/2011 at 15:19

Please note that [terms and conditions apply](#).

# Interfacial magnetic coupling between Fe nanoparticles in Fe–Ag granular alloys

J Alonso<sup>1</sup>, M L Fdez-Gubieda<sup>1</sup>, G Sarmiento<sup>1</sup>, J Chaboy<sup>2</sup>,  
R Boada<sup>2</sup>, A García Prieto<sup>3</sup>, D Haskel<sup>4</sup>, M A Laguna-Marco<sup>4</sup>,  
J C Lang<sup>4</sup>, C Meneghini<sup>5</sup>, L Fernández Barquín<sup>6</sup>, T Neisius<sup>7</sup> and  
I Orue<sup>8</sup>

<sup>1</sup> Departamento de Electricidad y Electrónica, Universidad del País Vasco (UPV/EHU), Campus de Leioa, 48940 Leioa, Spain

<sup>2</sup> Instituto de Ciencia de Materiales de Aragón, Consejo Superior de Investigaciones Científicas, CSIC—Universidad de Zaragoza, 50009 Zaragoza, Spain

<sup>3</sup> Departamento de Física Aplicada I, Escuela Universitaria de Ingeniería Técnica de Minas y de Obras Públicas, Universidad del País Vasco (UPV/EHU), 48902 Barakaldo, Spain

<sup>4</sup> Advanced Photon Source, Argonne National Laboratory, Argonne IL 60439, USA

<sup>5</sup> Dipartimento di Fisica ‘E Amaldi’, Università degli Studi Roma Tre, 00146 Roma, Italy

<sup>6</sup> CITIMAC, Universidad de Cantabria, Avenida de los Castros s/n, 39005 Santander, Spain

<sup>7</sup> Fédération de recherche des Sciences Chimiques de Marseille, Université Paul Cezanne, Campus St Jérôme, 13397 Marseille cedex 20, France

<sup>8</sup> SGIker, Universidad del País Vasco (UPV/EHU), Campus de Leioa, 48940 Leioa, Spain

Received 11 May 2011, in final form 7 November 2011

Published 14 December 2011

Online at [stacks.iop.org/Nano/23/025705](http://stacks.iop.org/Nano/23/025705)

## Abstract

The role of the interface in mediating interparticle magnetic interactions has been analysed in Fe<sub>50</sub>Ag<sub>50</sub> and Fe<sub>55</sub>Ag<sub>45</sub> granular thin films deposited by the pulsed laser deposition technique (PLD). These samples are composed of crystalline bcc Fe (2–4 nm) nanoparticles and fcc Ag (10–12 nm) nanoparticles, separated by an amorphous Fe<sub>50</sub>Ag<sub>50</sub> interface, occupying around 20% of the sample volume, as determined by x-ray diffraction (XRD), x-ray absorption spectroscopy (XAS), and high resolution transmission electron microscopy (HRTEM). Interfacial magnetic coupling between Fe nanoparticles is studied by dc magnetization and x-ray magnetic circular dichroism (XMCD) measurements at the Fe K and Ag L<sub>2,3</sub> edges. This paper reveals that these thin films present two magnetic transitions, at low and high temperatures, which are strongly related to the magnetic state of the amorphous interface, which acts as a barrier for interparticle magnetic coupling.

(Some figures may appear in colour only in the online journal)

## 1. Introduction

The physical properties of nanostructures can be markedly different from those of bulk materials. This is especially the case for magnetic materials, since nanometric structures lie in the length scale characteristic of the correlation lengths of the interactions involved [1, 2]. Often, the reduction of the particles' scale also implies structural modifications of these systems, through variations in the crystallographic state or the nanometric interfaces. These modifications strongly affect their magnetic response because of the strong interplay between structural disorder/defects, electronic structure, and conduction electron scattering. Striking phenomena may

also occur when the length scale reaches a few nanometres, such as giant magnetoresistance [3, 4] or magnetic coupling through non-magnetic spacers [5, 6]. These phenomena are of particular significance for granular alloys composed of magnetic clusters embedded in a metallic non-magnetic matrix where the interface between the clusters and the matrix plays a crucial role in determining the magnetotransport [7–9], magnetic moment [10] and magnetic interactions [11–13].

Concerning interparticle magnetic interactions, it has been observed that, as the concentration of the magnetic material in the granular alloys increases, the magnetic interactions become more relevant and give rise to different global magnetic behaviours of the system: (i) at low concentrations, magnetic

nanoparticles are well separated and therefore predominant interactions are of long range nature, such as dipolar or Ruderman–Kittel–Kasuya–Yosida (RKKY) [14]; (ii) as the number and/or size of the nanoparticles increases, they become closer together, and stronger short range interactions appear, such as direct exchange or tunnelling exchange interactions. Achieving a reliable and detailed understanding of these interactions is important, in order to fully exploit these systems and to tailor new innovative materials such as high-performance magnets [15, 16].

Granular systems consisting of magnetic nanoparticles (Fe, Co, Ni etc) embedded in a noble metal matrix (Cu, Ag or Au) constitute ideal candidates to study the role of the interactions in modifying the magnetic and magnetotransport properties of the system. These properties have been widely studied as a function of the magnetic particle size and concentration [4, 11, 13, 17–21]. However, little is known regarding the effect of the interface upon the exchange correlation length and magnetic coupling between the nanoparticles. Pulsed laser deposition (PLD) provides a unique method for probing interface effects in such systems since the energies reached during the preparation are high enough to allow some miscibility between the Fe grains and the Ag matrix. This has been, for example, observed in PLD Fe/Ag multilayers where a metastable Fe–Ag alloy of a few nanometres is obtained between the different layers [22, 23].

In this paper we present a study of the magnetic behaviour of the interface between the magnetic nanoparticles, shedding light on how it modifies the magnetic interactions between the nanoparticles, in the particular case of  $\text{Fe}_x\text{Ag}_{100-x}$  granular thin films. More specifically, we have analysed the role of the interface in mediating direct exchange interactions between the nanoparticles. Since these interactions are only intense when the magnetic nanoparticles are close together (touching or nearly touching), we have focused on the range of concentrations:  $x = 50\text{--}55$ , high enough to assure that the predominant interactions are of the exchange type, but not high enough for the nanoparticles to conglomerate as an ensemble, making it very difficult to differentiate them and hence to reach a clear conclusion. The structure of this interfacial region has been directly observed by high resolution transmission electron microscopy (HRTEM) and further explored by x-ray absorption spectroscopy (XAS) at the Fe K edge. Its magnetic behaviour and its influence on the magnetic interactions between nanoparticles has been studied by means of dc magnetometry, as a function of temperature and magnetic field, and further analysed with element-specific x-ray magnetic circular dichroism (XMCD) measurements at the Fe K edge and Ag  $L_{2,3}$  edges.

## 2. Experimental details

$\text{Fe}_{50}\text{Ag}_{50}$  and  $\text{Fe}_{55}\text{Ag}_{45}$  thin films have been prepared by the pulsed laser deposition technique (PLD). A rotating disc divided into sectors of Fe and Ag was ablated by a Kr–F excimer laser operated at a wavelength of 248 nm with a fluency at the target of  $2\text{--}3 \text{ J cm}^{-2}$ . The process was carried out in a vacuum less than  $10^{-5}$  mbar. The thin films were

deposited at 300 K onto Si(100) substrates, using an Al mask on the substrate in order to obtain samples of appropriate sizes according to the different techniques employed:  $3 \times 3 \text{ mm}^2$  squares for the magnetization measurements,  $5 \times 3 \text{ mm}^2$  squares for the XAS, XMCD, and HRTEM measurements, and a bigger piece of  $1 \times 1 \text{ cm}^2$  for XRD measurements. After deposition, the films were covered with  $\sim 10$  nm of Ag to prevent oxidation. The thicknesses of the thin films (200–250 nm) were measured by atomic force microscopy (Nanotec AFM). This allows us to estimate the volume of the sample, and thereby to obtain absolute magnetization values. Cu  $K\alpha$  x-ray diffraction was carried out on a Philips PW1710 diffractometer in the Bragg–Brentano geometry. The high resolution electron micrographs were collected on a Fei Titan 80–300 electron microscope (300 kV) at the Université Paul Cezanne (Marseille). The electron energy was 300 keV, with a resolution limit better than 1 Å. XAS measurements were carried out at the BM29 beamline of the European Synchrotron Radiation Facility (ESRF–Grenoble). All the spectra were obtained in a fluorescence setup and the measurements were carried out at room temperature, around the Fe K-edge energy (7112 eV), using a Si(111) monochromator, and reaching a maximum energy of  $k = 13 \text{ \AA}^{-1}$  ( $\sim 7756$  eV). Magnetic measurements were carried out using a SQUID magnetometer. Both zero field cooling (ZFC) and field cooling (FC) data were collected. For the ZFC data, the sample was cooled from room temperature down to 5 K, and then the magnetization was recorded with increasing temperature while applying a constant magnetic field. For the FC data, the process was repeated with the magnetic field applied while cooling. Magnetization measurements were taken in the temperature range 5–300 K with applied fields of  $H = 5, 10, 15$  and 25 Oe. The evolution of the magnetization as a function of the applied field at constant temperature was also analysed by measuring the hysteresis cycles,  $M(H)$ , with applied fields up to  $H = 65$  kOe. The XMCD experiments were performed at beamline 4-ID-D of the Advanced Photon Source at Argonne National Laboratory. Undulator radiation was monochromatized with double Si(111) crystals and its polarization converted from linear to circular with a diamond (111) quarter-wave plate operated in Bragg transmission geometry. Fluorescence XMCD spectra were recorded at the Fe K- and Ag  $L_{2,3}$  edges in grazing incidence geometry at different fixed temperatures from 320 down to 175 K. All measurements were carried out for two directions of the applied magnetic field (300 Oe), along and opposite to the incident photon wavevector, to check for systematic errors in the XMCD signals.

## 3. Results and discussion

### 3.1. Microstructure

**3.1.1. X-ray diffraction (XRD).** X-ray diffraction (XRD) measurements were used to characterize the microstructure of the samples. Figure 1 shows the Cu  $K\alpha$  x-ray diffractograms for Fe and  $\text{Fe}_{50}\text{Ag}_{50}$  thin films. In the case of the Fe film, only one very intense peak corresponding to the bcc Fe(110) Bragg reflection is observed, indicating that the Fe is highly textured

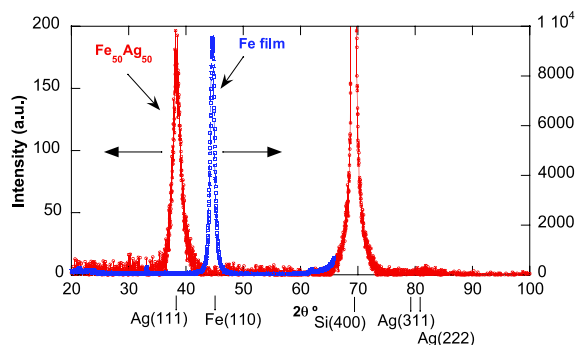


**Figure 1.** X-ray diffractograms from a  $\text{Fe}_{50}\text{Ag}_{50}$  (red circles) and a pure Fe (blue squares) film. The theoretical positions of the expected Bragg peaks are indicated below the  $2\theta$  axis.

in the (110) direction, typical for the growth of thin films with a bcc structure [24, 25].

The diffractogram of the  $\text{Fe}_{50}\text{Ag}_{50}$  film, on the other hand, does not display any peaks indicative of a pure Fe phase in the sample. This, however, does not rule out the presence of very small Fe nanoparticles of around a few nanometres. The x-ray diffraction pattern has two clear peaks: the first one ( $\sim 69^\circ$ ) corresponds to the Si(400) substrate Bragg diffraction, and the second one ( $\sim 38^\circ$ ) corresponds to the fcc Ag(111) Bragg peak. Two additional small Bragg peaks can be distinguished at higher angles ( $\sim 77^\circ$  and  $81^\circ$ ), which can be indexed with the fcc Ag(311) and (222) Bragg diffractions. The presence of a very intense (111) Bragg peak for the Ag, with very weak (311) and (222) peaks, suggests the Ag matrix is highly textured in the (111) direction, as generally observed in Fe–Ag thin films [4, 26, 27].

**3.1.2. High resolution transmission electron microscopy (HRTEM).** Figure 2 shows the high resolution transmission electron microscopy (HRTEM) images for the  $\text{Fe}_{50}\text{Ag}_{50}$  thin film. The obtained images have been analysed using the *ImageJ* software [28]. Interplanar spacings could be directly determined from the images, by measuring the lattice fringes. In addition, fast Fourier transform (FFT) was also performed on the HRTEM images of single particles, allowing us to identify the families of diffracting planes in that region. The identification of the phases can be quite complicated since both Fe and Ag belong to the cubic system, and some of the measured reflections do overlap [4, 29, 30]. The texture direction obtained from the XRD measurements, however, allows us to assign features in the HRTEM to specific phases (figure 2). An interplanar spacing  $\sim 2.4 \text{ \AA}$  (spots 1, 2) corresponding to fcc Ag(111) planes and  $\sim 2.1 \text{ \AA}$  (spots 3, 4) corresponding to bcc Fe(110) planes were obtained, both by direct measurements and FFT methods. The Fe nanoparticles present a bcc structure and average sizes between 2 and 4 nm. On the other hand, Ag nanograins have an fcc structure and are generally bigger, with diameters close to 10–12 nm.

More interesting is the fact that, apart from the crystalline nanoparticles, as indicated in figure 2, an amorphous region in which the nanoparticles are embedded can be clearly distinguished. Such an interface occupies around 20% of

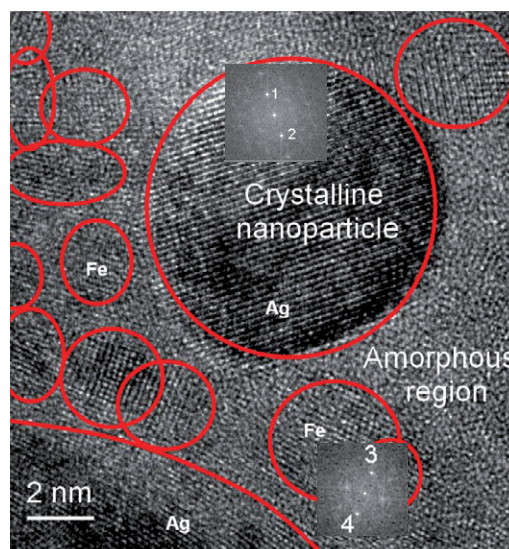


**Figure 2.** High resolution transmission electron micrograph obtained for an  $\text{Fe}_{50}\text{Ag}_{50}$  sample. Ellipsoids mark the positions of some crystalline nanoparticles. The insets correspond to the FFT of a Ag and an Fe nanoparticle.

the image, having a length scale between 1 and 3 nm, in agreement with the values reported for atomic mixing during laser deposition in Fe/Ag multilayers [22, 23].

**3.1.3. X-ray absorption spectroscopy (XAS).** The X-ray absorption spectroscopy (XAS) technique is a very powerful technique for resolving the local structure surrounding a particular atom. Traditionally, XAS is divided into two regions: (1) the low energy region called the x-ray absorption near-edge structure (XANES) and (2) the higher energy region, called the extended absorption fine structure (EXAFS). The EXAFS measurement allows the identification of the nearest neighbouring atoms to the absorbing atom to determine the coordination environment for the atom of interest. In our case, EXAFS at the Fe K edge was used to finely probe the average local atomic environment around the Fe atoms, both inside the Fe nanoparticles, and inside the Fe–Ag amorphous interface. Figure 3 shows the XAS spectra obtained for the  $\text{Fe}_{50}\text{Ag}_{50}$  and Fe thin films, the latter used as reference. The shapes of the two spectra are qualitatively comparable, presenting similar fine structure oscillations, although appreciably damped in the case of the  $\text{Fe}_{50}\text{Ag}_{50}$  sample. Further, no pre-edge peaks are observed in these spectra, indicating that there is little or no Fe oxidation in either sample.

The EXAFS functions were extracted from the absorption spectra using standard procedures [31] for data normalization. In figure 4 we plot the  $k^3$  weighted EXAFS spectra,  $k^3\chi(k)$ , and their corresponding Fourier transform, FT, obtained in the  $k$  range  $3.5 \text{ \AA}^{-1} < k < 13 \text{ \AA}^{-1}$ , using a Hanning window function, for  $\text{Fe}_{50}\text{Ag}_{50}$  and Fe thin films. The Fourier transform of  $\chi(k)$  for the  $\text{Fe}_{50}\text{Ag}_{50}$  sample presents the main features of a bcc structure but some differences can be observed with respect to the Fe thin film. First, the  $\chi(k)$  and FT amplitudes are considerably weaker in the  $\text{Fe}_{50}\text{Ag}_{50}$  sample. Moreover,

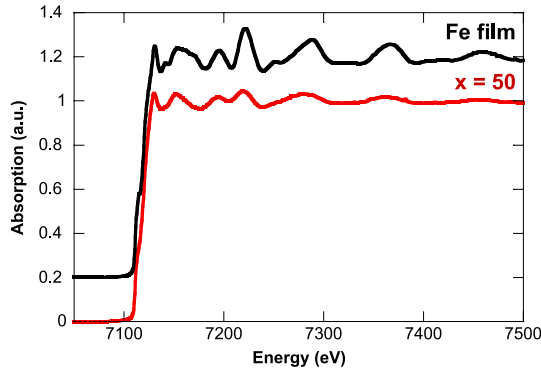


**Figure 3.** Normalized XAS spectra for a  $\text{Fe}_{50}\text{Ag}_{50}$  sample (red line) and a pure Fe film (black line).

there is an increasing reduction of the amplitude ratio of the FT peaks with increasing  $R$ , this being particularly pronounced for the third peak. Additionally, the position of the first peak in the Fourier transform (not phase corrected) is slightly shorter for the  $\text{Fe}_{50}\text{Ag}_{50}$ , being around  $2.22 \text{ \AA}$  for the Fe film and  $2.16 \text{ \AA}$  for the  $\text{Fe}_{50}\text{Ag}_{50}$ . Finally, the shape of next neighbour peaks is slightly different in Fe and  $\text{Fe}_{50}\text{Ag}_{50}$  data, indicating some different local structure around Fe in the two samples.

In order to obtain quantitative information, we have fitted the experimental spectra using the standard EXAFS formula:

$$k\chi(k) = \sum_j S_0^2 N_j f_j(k) \frac{e^{-2\sigma_j^2 k^2} e^{-2\Gamma_j/k}}{R_j^2} \sin[2kR_j + \varphi_j(k)] \quad (1)$$

which assumes a discrete lattice where  $R_j$  is the mean distance between the absorber atom and the scattering neighbour  $j$ ,  $N_j$  is the coordination number, and  $\sigma_j^2$  is the mean square displacement of the Gaussian pair distribution function, due to thermal and static disorder. The backscattering amplitude and phase functions,  $f_j(k)$  and  $\varphi_j(k)$ , the photoelectron mean free path,  $\Gamma_j$ , and the empirical parameter,  $S_0^2$ , associated with

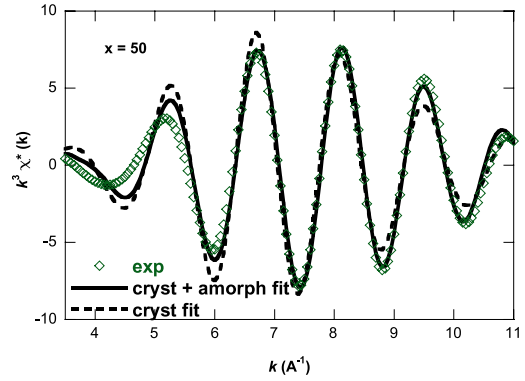


**Figure 5.** Inverse Fourier transform of FT,  $k^3 \chi^*(k)$ , for the main peak,  $1 \text{ \AA} \leq R \leq 3 \text{ \AA}$  of an  $\text{Fe}_{50}\text{Ag}_{50}$  sample. Black lines correspond to the fittings of the spectra using a crystalline + amorphous model (continuous line), and a crystalline model (discontinuous line).

many body losses were obtained from the FEFF8.4 code [32]. In the case of the Fe film, we have fitted the EXAFS spectrum,  $\chi(k)$ , in the  $k$  range  $3.5 \text{ \AA}^{-1} < k < 13 \text{ \AA}^{-1}$ . The  $N_j$  parameters were constrained to the bcc Fe coordination numbers while the  $R_j$  parameters have been left free to vary independently around the bcc Fe positions. Six contributions are required for a satisfactory refinement: four single scattering paths from the absorbing Fe atom to its neighbours in the first to fourth shells, and two collinear focusing double and triple scattering paths along the bcc cell diagonal. The results of the analysis are presented in table 1, and the quality of the fit can be observed in figure 4. Attempts to refine the  $\text{Fe}_{50}\text{Ag}_{50}$  sample EXAFS signal using the above procedure gave unsatisfactory fit, as depicted in figure 5, showing the inverse Fourier transform,  $\chi^*(k)$ , of the first peak of FT ( $1 \text{ \AA} \leq R \leq 3 \text{ \AA}$ ), together with the fit (discontinuous line). This discrepancy must be ascribed to the presence of Fe in the amorphous interface detected by HRTEM.

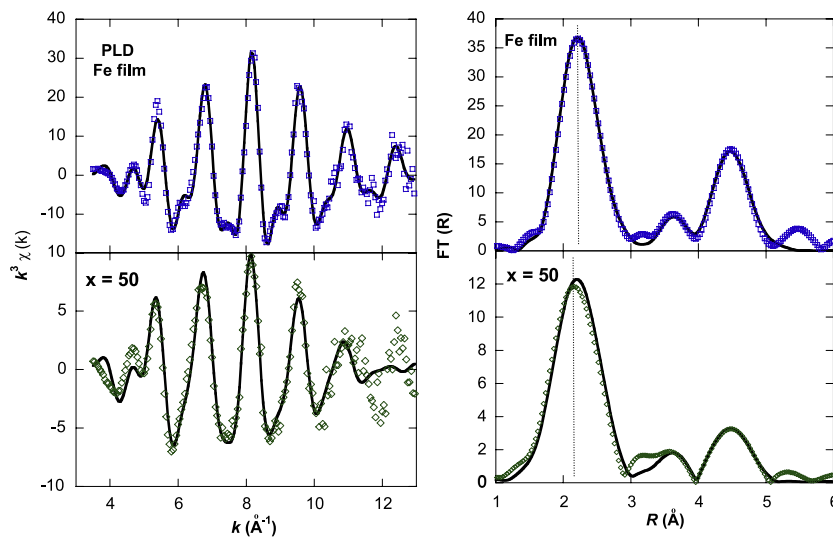


**Figure 4.** EXAFS spectra,  $\chi(k)$ , and the corresponding Fourier transform moduli,  $\text{FT}(R)$ , for a  $\text{Fe}_{50}\text{Ag}_{50}$  and a pure Fe film. Black lines correspond to the fittings of the spectra.

**Table 1.** Values of structural parameters: interatomic distances,  $R_j$ , Debye–Waller factors,  $\sigma_j^2$ , mean deviation interatomic distances,  $\sigma_{Dj}$ , and average interatomic distances,  $\bar{R} = R_j + \sigma_{Dj}$ .

	Crystalline phase							
	$R_1$ (Å)	$R_2$ (Å)	$R_3$ (Å)	$R_4$ (Å)	$\sigma_1^2$ (Å <sup>2</sup> )	$\sigma_2^2$ (Å <sup>2</sup> )	$\sigma_3^2$ (Å <sup>2</sup> )	$\sigma_4^2$ (Å <sup>2</sup> )
Fe film	2.46(1)	2.84(2)	4.05(4)	4.76(1)	0.005(1)	0.007(2)	0.01(5)	0.007(2)
$x = 50$	2.46	2.84	4.06(6)	4.78(3)	0.009(3)	0.009(3)	0.02(1)	0.02(1)
	Amorphous phase							
	$R_{\text{Fe-Fe}}$ (Å)	$\sigma_{D\text{Fe-Fe}}$ (Å)	$\bar{R}_{\text{Fe-Fe}}$ (Å)	$R_{\text{Fe-Ag}}$ (Å)	$\sigma_{D\text{Fe-Ag}}$ (Å)	$\bar{R}_{\text{Fe-Ag}}$ (Å)		
$x = 50$	2.56(9)	0.04(4)	2.6(1)	2.88(9)	0.03(4)	2.9(1)		

Therefore, we have included the amorphous contribution by adding a new term to equation (1), in which a general approximation in terms of a partial radial distribution function  $h_j(r)$  is considered. The new term can be expressed as [31, 33]

$$k\chi(k) = \sum_j S_0^2 N_j f_j(k) \int \frac{e^{-2\Gamma_j/k}}{r^2} h_j(r) \sin[2kr + \varphi_j(k)] dr \quad (2)$$

where  $h_j(r)$  is the convolution of a Gaussian function,  $P_G(r)$ , centred at  $R_j = 0$ , with a mean square width,  $\sigma_j^2$ , and an asymmetry function,  $g_j(r)$ , given by

$$g_j(r) = \frac{1}{\sigma_{Dj}} e^{-\frac{r-R_j}{\sigma_{Dj}}}, \quad \text{for } r \geq R_j \quad (3)$$

$$g_j(r) = 0, \quad \text{for } r < R_j$$

proposed by De Crescenzi *et al* [34] in the framework of the dense random packing of hard spheres model. In this model,  $R_j$  becomes the distance between the centres of two touching spheres and  $\sigma_{Dj}$  is the root mean square deviation of the distance between the absorbing atom and the neighbour  $j$ . The average distance will then be given by  $\bar{R} = R_j + \sigma_{Dj}$ . By introducing  $h_j(r) = P_G(r) \otimes g_j(r)$  in (2), we obtain the following expression:

$$k\chi(k) = \sum_j S_0^2 N_j f_j(k) \frac{e^{-2\sigma_j^2 k^2} e^{-2\Gamma_j/k}}{R_j^2} \frac{1}{\sqrt{1 + 4k^2 \sigma_{Dj}^2}} \times \sin[2kR_j + \arctan(2k\sigma_{Dj}) + \varphi_j(k)]. \quad (4)$$

This expression has proved to be very useful in the analysis of amorphous alloys, such as  $(\text{Fe}_{0.2}\text{Co}_{0.8})_{75}\text{Si}_x\text{B}_{25-x}$ , Co–P or Fe–B [35–38]. Therefore, we have fitted the EXAFS spectrum for the  $\text{Fe}_{50}\text{Ag}_{50}$  sample, in the  $k$  range  $3.5 \text{ \AA}^{-1} < k < 11 \text{ \AA}^{-1}$ , using a weighted sum of both equations (1) and (4):

$$k\chi(k) = p(\text{equation (1)}) + (1 - p)(\text{equation (4)}). \quad (5)$$

In order to reduce the number of free parameters and the correlations between them we applied some constraints. Concerning the crystalline contribution, we used the same criteria as employed for the Fe film and we fixed  $S_0^2$  and the interatomic distances of the first two shells,  $R_1$  and  $R_2$ , to the values obtained for the Fe film. We also constrained  $N_j$  to the bcc Fe coordination numbers. To represent

the amorphous contribution, we have considered a structure consisting of an absorbing Fe atom, and a single coordination shell composed of 12 neighbouring atoms of Fe and/or Ag. In this way, in the amorphous region, there are two possible paths for the backscattering: Fe–Fe and Fe–Ag. Each of these paths has a Debye–Waller parameter assigned,  $\sigma_j^2$ , and the average interatomic distance is given by  $\bar{R} = R_j + \sigma_{Dj}$ . Additionally, we have let the relative proportion of Fe and Ag neighbouring atoms in this amorphous region vary around 50/50, as suggested by magnetic measurements (see below).

In table 1 we present the values of the different fitting parameters, and the quality of the fit,  $(\chi_{\text{exp}} - \chi_{\text{th}})^2 / \chi_{\text{exp}}^2 = 0.06$ , can be observed in figures 4 and 5 (continuous line). The obtained  $\sigma_j^2$  values for the Fe–Fe and Fe–Ag paths in the amorphous phase are 0.004(4) and 0.010(5), respectively. The proportion of the amorphous Fe–Ag interface is around 25%, corroborating the HRTEM results ( $\approx 20\%$ ), and its composition is close to  $\text{Fe}_{50}\text{Ag}_{50}$ . Fe–Fe and Fe–Ag average distances in the amorphous interface are  $\sim 2.6$  and  $2.9 \text{ \AA}$ , respectively.

To sum up, XRD, HRTEM and EXAFS techniques have essentially revealed that the  $\text{Fe}_{50}\text{Ag}_{50}$  granular thin film is composed of  $\sim 80\%$  crystalline Fe nanoparticles + Ag nanoparticles (in an atomic proportion 50/50), and  $\sim 20\%$  of a  $\text{Fe}_{50}\text{Ag}_{50}$  amorphous alloy, which surrounds the nanoparticles. Fe nanoparticles have a highly textured bcc structure, with average sizes of 2–4 nm, and fcc Ag nanoparticles are also very textured, with sizes around 10–12 nm.

### 3.2. Magnetization results

Having obtained a clear description of the nanostructural characteristics of the samples, specially concerning the amorphous Fe–Ag interface, we can turn our attention to their magnetic response, in order to distinguish the role of the amorphous interface, and to understand how this interface affects the interparticle magnetic interactions. The ZFC/FC magnetization has been measured with an applied field of 5 Oe for  $\text{Fe}_{50}\text{Ag}_{50}$  and  $\text{Fe}_{55}\text{Ag}_{45}$  thin films, as shown in figure 6(a). For the ZFC data, the magnetization increases from 5 K up to  $T_{P1}$  ( $\sim 88 \text{ K}$  and  $49 \text{ K}$  for  $\text{Fe}_{50}\text{Ag}_{50}$  and  $\text{Fe}_{55}\text{Ag}_{45}$ , respectively), which is the temperature of the first shoulder in the ZFC curve, at which a clear change in the slope of the magnetization takes place. Then the ZFC magnetization follows a smooth evolution characteristic of a ferromagnetic state up to  $T_{P2}$  ( $\sim 201$  and  $172 \text{ K}$  for  $\text{Fe}_{50}\text{Ag}_{50}$  and  $\text{Fe}_{55}\text{Ag}_{45}$ , respectively),

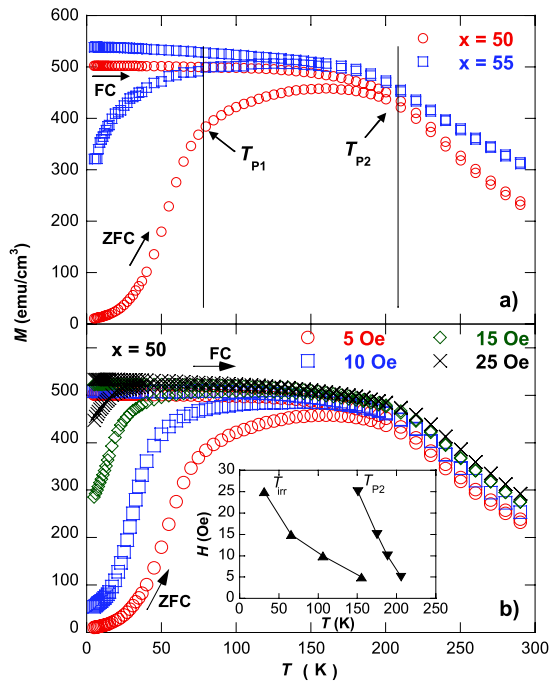


**Figure 6.** (a)  $M^{\text{ZFC}}$  and  $M^{\text{FC}}$  versus temperature for an  $\text{Fe}_{50}\text{Ag}_{50}$  (circles) and an  $\text{Fe}_{55}\text{Ag}_{45}$  (squares) thin film, with  $H = 5$  Oe. (b)  $M^{\text{ZFC}}$  and  $M^{\text{FC}}$  versus temperature for an  $\text{Fe}_{50}\text{Ag}_{50}$  thin film at different applied magnetic fields  $H = 5, 10, 15$  and  $25$  Oe. Inset: evolution of  $T_{\text{irr}}$  and  $T_{\text{P}2}$  as a function of the magnetic field.

defined as the temperature at which the magnetization starts to decrease again, and signalled by a change in the curvature of the ZFC curve. Finally, the ZFC magnetization decreases following a Curie–Weiss law. On the other hand, the FC curve remains roughly constant with increasing temperature up to the irreversibility temperature,  $T_{\text{irr}}$ , which is the temperature at which the ZFC and FC curves overlap.

In order to understand the nature of these transitions,  $T_{\text{P}1}$  and  $T_{\text{P}2}$ , we have measured the ZFC/FC curves under different applied magnetic fields,  $5 \text{ Oe} \leq H \leq 25 \text{ Oe}$ , for  $\text{Fe}_{50}\text{Ag}_{50}$  thin film. As can be seen in figure 6(b) the first transition is notably affected by the applied magnetic field. With increasing magnetic field, ZFC and FC curves tend to overlap, the irreversibility temperature,  $T_{\text{irr}}$ , displaces to lower temperatures and the transition  $T_{\text{P}1}$  tends to disappear. This behaviour is typical of glassy systems [14, 39] and suggests that the system enters a spin-glass-like state at low temperatures, that can be easily overcome by the application of an increasing magnetic field.

The second transition, above  $T_{\text{P}2}$ , is almost unaffected by the magnetic field, indicating that the magnetic disorder at these temperatures is more stable.

The inset of figure 6(b) represents the evolution of the irreversibility temperature,  $T_{\text{irr}}$ , and the transition temperature,  $T_{\text{P}2}$ , as a function of the magnetic field. This diagram resembles that of a re-entrant spin glass (see for example [14]) where the system evolves from a paramagnetic state to a ferromagnetic one, and finally to a spin-glass-like state as the temperature decreases. The shape of the ZFC/FC curves of the present sample is very similar to that observed in the case

of magnetically disordered systems, such as solid solutions or amorphous alloys [5, 6, 14, 40–43]. Chien *et al* [44] observed that Fe–Ag amorphous alloys with Fe concentrations around 45–50 at.% became paramagnetic above a Curie temperature in the range 200–250 K, close to  $T_{\text{P}2}$ . This finding suggests that the amorphous interface should be close to this composition, this being the reason why we constrained the EXAFS fitting of the amorphous interface to a 50/50 composition.

Considering these results, we propose that the amorphous Fe–Ag interface region in the samples gets magnetically ordered/disordered as a function of temperature, acting as a barrier for the magnetic coupling between the Fe nanoparticles. In the temperature range between  $T_{\text{P}1}$  and  $T_{\text{P}2}$ , this interface region is magnetically ordered, enabling direct exchange interactions between the nanoparticles, and supports the ferromagnetic order, resulting in a global ferromagnetic-like behaviour characterized by a smooth and roughly constant  $M(T)$  curve. Above  $T_{\text{P}2}$  the amorphous interface becomes paramagnetic, and this suppresses ferromagnetic exchange interactions between the Fe nanoparticles, giving rise to the decay of the global magnetization of the system. Below  $T_{\text{P}1}$  this interface region gets magnetically disordered in a spin-glass-like state, restricting the interparticle exchange coupling and, as a consequence, a reduction of the global magnetization is obtained.

The magnetic state of the interface also affects the magnetic response of the sample as a function of the magnetic field (hysteresis loops,  $M(H)$ ). Specifically, as shown in figure 7(a), the coercivity,  $H_{\text{C}}$ , of the  $\text{Fe}_{50}\text{Ag}_{50}$  thin film takes a value of 19.6 Oe at 5 K, then decreases to 8.9 Oe at 80 K and remains constant up to  $\sim 200$  K, where a sharp increase takes place, reaching a value of 28.8 Oe at 300 K. On the other hand the normalized remanence,  $M_{\text{r}}/M_{\text{S}}$ , is  $\sim 0.9$  up to  $T_{\text{P}2}$ , where it decreases to  $\sim 0.55$  near 300 K.

The evolution of  $H_{\text{C}}$  clearly follows that of the ZFC magnetic susceptibility. At low temperatures, the spin-glass-like disorder of the interface gives rise to a weak correlation between the nanoparticles. As the temperature rises to  $T_{\text{P}1}$ , this correlation increases and therefore the coercivity decreases. At  $T > T_{\text{P}1}$  the interface becomes ferromagnetic, coupling the nanoparticles, and as a consequence the coercivity remains nearly constant as temperature goes up, and the normalized remanence is very high, close to unity. Above  $T_{\text{P}2}$ , the amorphous Fe–Ag interface region is in a paramagnetic state, the magnetic nanoparticles decouple and hence the value of  $H_{\text{C}}$  increases, and  $M_{\text{r}}/M_{\text{S}}$  approaches the value of a non-interacting random anisotropy system, 0.5. A similar evolution for the coercivity has been obtained in Fe nanocrystals grown from an amorphous matrix [6, 42, 43].

Another remarkable result, shown in figure 7(b), is the appearance of a displacement of the hysteresis loop at low temperatures ( $-4.3$  Oe at 5 K, for the  $\text{Fe}_{50}\text{Ag}_{50}$  thin film), observed when cooling the sample at remanence. This trend is characteristic of exchange-biased systems and has been reported in other inhomogeneous materials [45], such as spin glass (FeAu)/NiFe thin films [46] or  $\text{Fe}_x\text{Zr}_{100-x}$  amorphous materials [47]. In the present case this effect must be a consequence of the spin-glass-like state of the

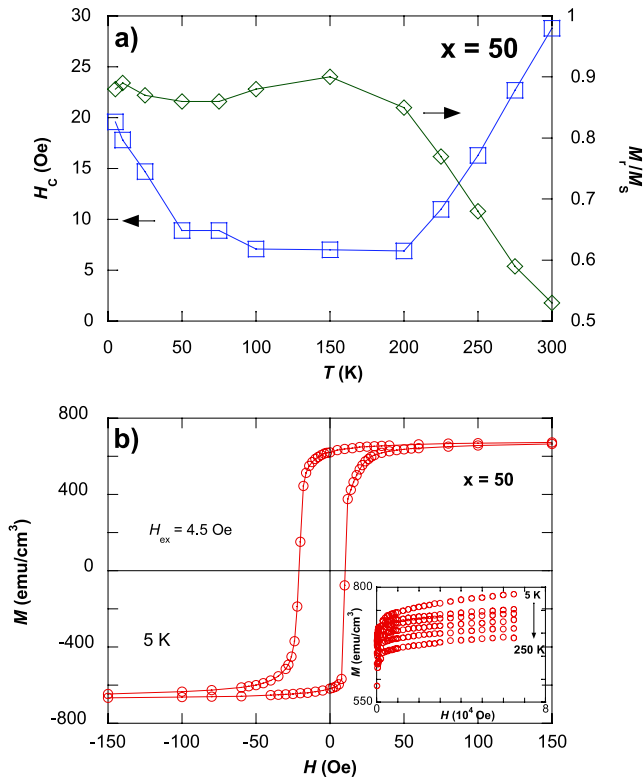


**Figure 7.** (a) Thermal evolution of the coercivity,  $H_c$ , and the normalized remanence,  $M_r/M_s$ , measured for an  $\text{Fe}_{50}\text{Ag}_{50}$  sample. (b) Hysteresis loop,  $M(H)$ , measured for the same sample after cooling in remanence. An exchange bias is clearly observed. In the inset,  $M(H)$  curves measured at 5, 30, 50, 85, 145, 200 and 250 K are plotted ( $H_{\text{max}} = 65 \text{ kOe}$ ).

amorphous interface: at low temperatures the magnetic moments at the surface of the nanoparticles freeze into a magnetically disordered state, acting as a torque anisotropy for the moments in the ferromagnetic core and hence playing the role of an antiferromagnetic surface around the ferromagnetic nanoparticle, which is the typical example of exchange-biased systems [48]. Another consequence of the spin-glass-like state at the interface is the unsaturated behaviour of the magnetization, even for high magnetic fields (65 kOe), which is particularly pronounced at low temperatures (5 K), as shown in the inset of figure 7(b). Even more, as depicted in the inset, the estimated value of the saturation magnetization,  $M_s$ , decays by  $\sim 10\%$  between 5 and 250 K. From this result, we can estimate the magnetic moment of the Fe atoms inside the amorphous Fe–Ag interface,  $\mu_{\text{int}}$ . Our previous findings showed that above  $T_{P2}$  ( $\sim 200 \text{ K}$ ) the amorphous interface, which occupies around 20% of the sample, became paramagnetic. Since the typical magnetic moment of bcc Fe atoms is  $2.2 \mu_B$ , the average magnetic moment of the Fe atoms in the  $\text{Fe}_{50}\text{Ag}_{50}$  film below the transition must be  $\mu_{T < T_{P2}} = 0.8 \times 2.2 \mu_B + 0.2 \times \mu_{\text{int}}$ , while above the transition, its value is  $\mu_{T > T_{P2}} = 0.8 \times 2.2 \mu_B$ . Since the average magnetic moment of Fe in the samples decreases by 10%, this means that  $\mu_{T > T_{P2}} = 0.9 \times \mu_{T < T_{P2}}$ , and thereby  $\mu_{\text{int}} = 0.97 \mu_B$ . Therefore, the Fe atoms inside this Fe–Ag interface present a notably reduced magnetic moment ( $0.97 \mu_B$ ), in comparison to those in a typical bcc environment ( $2.2 \mu_B$ ).

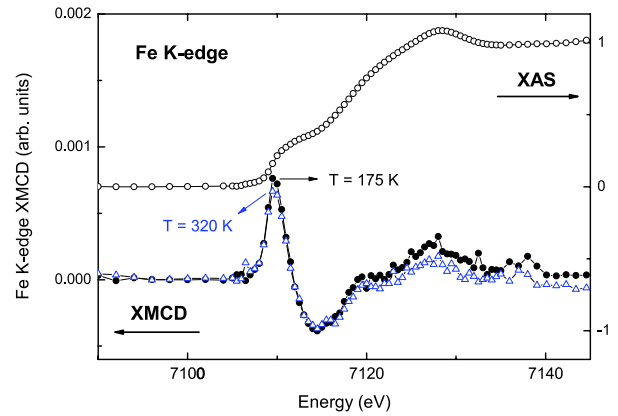


**Figure 8.** Comparison of the Fe K-edge XMCD spectra recorded on the  $\text{Fe}_{50}\text{Ag}_{50}$  thin film at temperatures below and above the magnetic transition:  $T = 175 \text{ K}$  (black,  $\bullet$ ) and  $T = 320 \text{ K}$  (blue, open triangles). For the sake of comparison the normalized Fe K-edge XANES spectrum recorded at  $T = 175 \text{ K}$  is also shown.

In order to help elucidate the role of the amorphous Fe–Ag interface in the magnetic moment, we have measured the Fe and Ag magnetization through the magnetic transition at  $T_{P2}$  ( $\sim 200 \text{ K}$ ), by performing an XMCD study at the Fe K and Ag  $L_{2,3}$  edges on an  $\text{Fe}_{50}\text{Ag}_{50}$  thin film. Measurements were performed applying a magnetic field of 300 Oe, well above the coercive field (see figure 7(b)). The XMCD spectra, figure 8, are very similar to those measured in bcc Fe metal [49, 50]: they show a narrow positive peak at the absorption threshold, a negative dip ( $\sim 12 \text{ eV}$  wide), and a broad positive resonance at higher energies. This spectral shape does not change as a function of the temperature and only the intensity of the main spectral features varies. In this way, the amplitude of the XMCD signal is larger at temperatures below the magnetic transition than above. This behaviour indicates that the magnetic moment of Fe decreases as the temperature rises through the transition. Estimates of the amplitude variation of the XMCD spectra yield that the magnetic moment of Fe above 200 K is reduced by  $\sim 10\%$  with respect to its value at low temperature. This is in agreement with the previously reported decay of the saturation magnetization,  $M_s$ .

In order to get deeper insight into the relationship between the magnetic transition around 200 K and the magnetic ordering/disordering of the Fe–Ag amorphous interface region, we have studied the magnetic behaviour of the Ag atoms in the granular films by XMCD measurements at the  $L_{2,3}$  edges of Ag through the transition. XMCD at  $L_{2,3}$  edges probes the empty 4d states of Ag. In principle Ag, in its atomic form, has completely filled 4d states, implying that there is no net magnetic moment. However, when Ag participates in a metallic alloy, hybridization can induce holes in the 4d band of Ag. Therefore a magnetic moment, even small, can be induced at the Ag sites. To our knowledge, the magnetic polarization of Ag by Fe atoms has been only proven in a few cases, such as  $\text{Ni}_{81}\text{Fe}_{19}/\text{Ag}$  coupled multilayers [51] and Fe/Ag compositionally modulated films [52]. By contrast, the magnetic polarization of 4d electrons by Fe atoms has been widely reported in the case of Pd/Fe multilayers [53] and

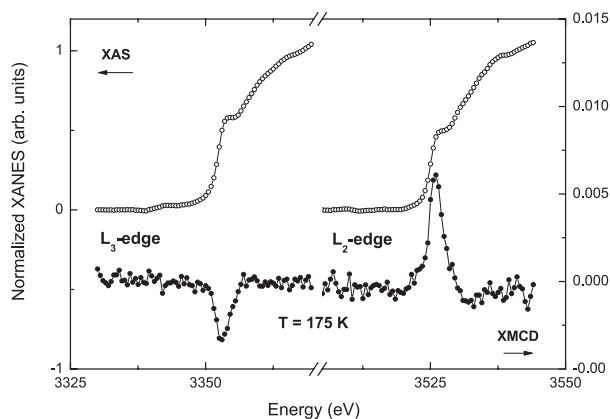


**Figure 9.** XANES (○) and XMCD (●) spectra recorded on the  $\text{Fe}_{50}\text{Ag}_{50}$  sample at the Ag  $L_{2,3}$  edges at  $T = 175$  K.

$\text{Fe}_{1-x}\text{Rh}_x$  alloys [54]. Similar results extend to the polarization of nominally non-magnetic atoms such as Ru, Ag, Cu and Au by Co in granular alloys and multilayers [10, 55, 56].

One of the main difficulties of studying the magnetic signal from noble metals at interfaces lies in the small magnitude of induced magnetic moments. Indeed, theoretical calculations predict that the Ag total induced magnetic moment at the Fe/Ag interface is only  $0.03 \mu_B$  [57]. Despite this small magnetic moment, an evident dichroic magnetic signal from Ag has been detected in the  $\text{Fe}_{50}\text{Ag}_{50}$  thin film. Figure 9 shows the XMCD spectra recorded at the Ag  $L_{2,3}$  edges of the film at  $T = 175$  K. The sign and magnitude of the observed signals are in agreement with previous observations by Jaouen *et al* [51]. Moreover, the sign of the XMCD signal recorded at the  $L_{2,3}$  edges and at the Fe K edge indicates that the coupling between the Fe magnetic moment and that induced in the Ag atoms is ferromagnetic.

Now the presence of a magnetic moment at the Ag sites has been demonstrated, we focus on the variation of this induced magnetic moment across the magnetic transition. As shown in figure 10 the amplitude of the Ag XMCD decreases as the temperature increases, following the global magnetic behaviour during the magnetic transition. However, the important point is to quantify the relative variation of the Ag induced moment across the transition. While the reduction of the Fe magnetic moment through the transition is 10%, the reduction of the Ag one reaches 20% of the value at  $T = 175$  K. This is in agreement with the fact that the Fe–Ag amorphous interface, which occupies around 20% of the sample, becomes paramagnetic above 200 K, and therefore, the Fe atoms inside this Fe–Ag alloy no longer polarize the neighbouring Ag atoms. However, the magnetic moment of the Ag is far from being zero even at 320 K. It is important to remember that the Fe–Ag thin films are composed of 80% of Fe nanoparticles + Ag nanoparticles (in a 50/50 atomic proportion), and 20% of  $\text{Fe}_{50}\text{Ag}_{50}$  amorphous alloy. This indicates that there are still polarized Ag atoms, which we have associated with those in direct contact with the surface atoms of the crystalline Fe nanograins and clusters, both inside the amorphous interface and on the surface of some crystalline Ag nanograins.

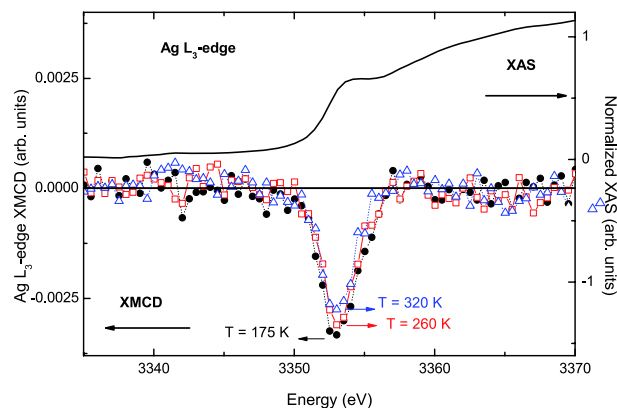


**Figure 10.** Ag  $L_3$  XMCD spectra as a function of the temperature:  $T = 175$  K (black, ●),  $T = 260$  K (red, open squares) and  $T = 320$  K (blue, open triangles).

Finally, it is instructive to compare the magnitude of the induced Ag XMCD signal to that reported by Jaouen *et al* in Ag/ $\text{Ni}_{80}\text{Fe}_{20}$  multilayers [51]. It was found that 1 nm Ag layers were nearly uniformly polarized by interfacial proximity to the permalloy with a magnetic moment of approx.  $0.015 \mu_B/\text{Ag}$  atom. This polarization yields a 1.2% Ag XMCD signal, compared to the 0.3% reported here (reduction factor of 4). This probably indicates that not all Ag atoms are polarized in our sample, especially when one considers that the magnetization of  $\text{Ni}_{80}\text{Fe}_{20}$  is half that of Fe (although the interfacial electronic structure ought to be considered). Polarization of only a fraction of the Ag atoms in our sample is not surprising. First, our Ag crystalline nanoparticles are  $2R = 11$  nm in diameter, compared to the 1 nm layers in the work by Jaouen *et al*. Assuming a  $dR = 0.2$  nm interfacial region polarized by proximity to crystalline Fe, the fraction of polarized Ag atoms in the crystalline nanoparticles is 11%. Since the crystalline regions occupy 80% of the sample volume, one would expect at least a factor of 11 ( $1/(0.8 \times 0.11)$ ) reduction in Ag XMCD signal relative to that reported by Jaouen *et al*, if only Ag atoms in the crystalline nanoparticles are polarized. The much smaller reduction (factor 4) in Ag XMCD provides evidence for the presence of polarized Ag atoms outside the crystalline regions, i.e. within the amorphous  $\text{Fe}_{50}\text{Ag}_{50}$  regions, which occupy 20% of the sample volume. For example, accounting for the relative contributions of crystalline (80%) and amorphous (20%) regions together with their fractional polarization, we get  $(0.8 \times 0.11 + 0.2 \times 1) = 0.29$ , or a factor of 3.5 reduction in Ag XMCD, close to the observed reduction factor of 4. Although qualitative in nature, especially considering the uncertainty arising from possible dissimilar electronic structures at Ag–Fe and Ag– $\text{Ni}_{80}\text{Fe}_{20}$  interfaces/alloys, the analysis above indicates that the Ag XMCD signal is likely to have sizeable contributions from both interfacial and amorphous regions. Furthermore, the moderate (20%) reduction in Ag XMCD observed when the amorphous regions transition from an FM to a PM state provides additional evidence that a sizeable contribution from polarized Ag atoms in crystalline regions must be present, as these atoms remain polarized due to their proximity to high  $T_C$  (1025 K) crystalline Fe regions.

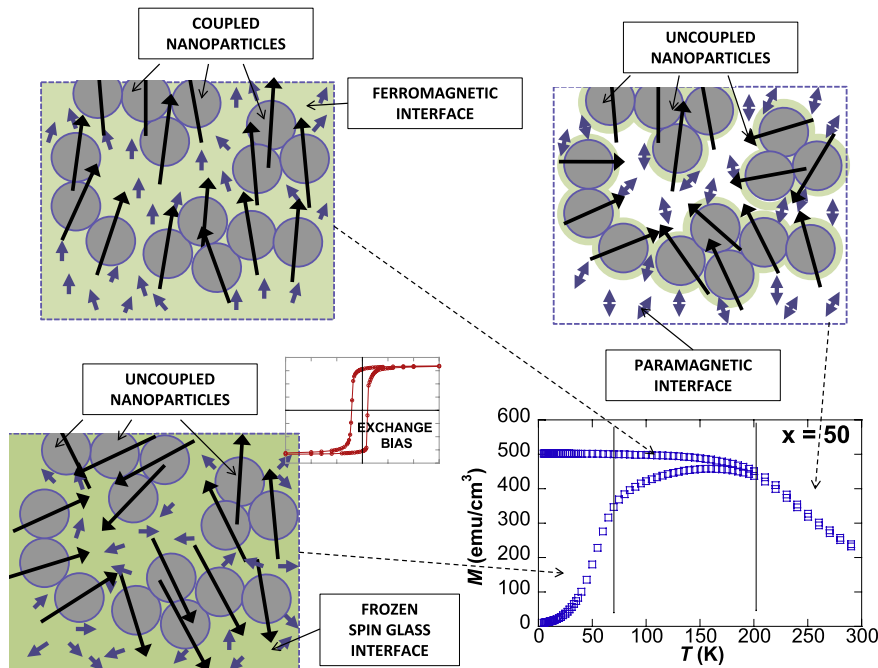


**Figure 11.** Picture of the thermal evolution of the magnetic structure for a laser ablated  $\text{Fe}_{50}\text{Ag}_{50}$  thin film. Simplified pictures of the magnetic moment configurations in three ranges of temperature are also included. The coloured background indicates the presence of polarized Ag atoms inside the amorphous Fe–Ag interface. Ag nanoparticles, although present, have not been drawn for clarity.

### 3.3. Conclusions

In  $\text{Fe}_x\text{Ag}_{100-x}$  ( $x = 50\text{--}55$ ) thin films prepared using pulsed laser deposition it is possible to define and manipulate the Fe–Ag interface in order to tune the interparticle magnetic interactions through a very attractive structural arrangement. The nanostructure has been revealed by x-ray diffraction (XRD), high resolution transmission electron microscopy (HRTEM) and x-ray absorption spectroscopy (XAS) showing that the metallic films consist of bcc Fe nanoparticles (2–4 nm) and fcc Ag nanoparticles (10–12 nm), surrounded by an amorphous interface, consisting of an  $\text{Fe}_{50}\text{Ag}_{50}$  alloy, which occupies around 20% of the sample volume.

Magnetic measurements indicate a re-entrant spin-glass-like (RSG) behaviour as a function of temperature, with two magnetic transitions taking place at high and low temperatures, as evidenced by the sudden decrease of the  $M(T)$  curves in both cases. We have determined that these transitions are mediated by the magnetic ordering/disordering of the amorphous Fe–Ag interface that surrounds the nanoparticles. To throw light on the evolution of the interparticle coupling mechanism, figure 11 shows some schematic pictures in conjunction with the experimental thermal magnetization variation for a laser ablated  $\text{Fe}_{50}\text{Ag}_{50}$  (Ag nanoparticles are not drawn to clarify the global magnetic behaviour). These schematic pictures describe the magnetic state of the Fe nanoparticles for different ranges of temperatures:

- (i) At low temperatures,  $T < 65$  K, the amorphous  $\text{Fe}_{50}\text{Ag}_{50}$  interface, which separates the magnetic nanoparticles, is frozen in a spin-glass-like state, as revealed by the presence of an exchange bias phenomenon in the

hysteresis loop and the unsaturated magnetic behaviour. Direct exchange interactions between the Fe nanoparticles are blocked, and their magnetic moments are globally disordered.

- (ii) At intermediate temperatures,  $70 \text{ K} < T < 205 \text{ K}$ , the amorphous interface is ferromagnetically ordered, enabling the direct exchange between the nanoparticles. At these temperatures, XMCD data reveal a clear polarization of the Ag atoms.
- (iii) At high temperatures ( $T > 210 \text{ K}$ ), the amorphous interface becomes paramagnetic and, therefore, the direct exchange between the nanoparticles is again disabled, and the magnetization of the system decreases. As a result, the average magnetic moment of the Fe atoms is reduced by 10%, as revealed by XMCD and magnetization measurements, which indicates that the Fe atoms inside this amorphous interface have a small magnetic moment ( $0.97 \mu_B$ ). On the other hand, the average magnetic moment of the Ag atoms decreases by 20%, in agreement with the amount of amorphous region in the sample. However, there is still an appreciable number of polarized Ag atoms, which we have associated with those in direct contact with the surface atoms of the crystalline Fe nanograins and clusters.

It is expected that this study, which involves nanomagnetic crystallites embedded in an amorphous interface allowing the triggering and enhancement of intergrain coupling, will motivate the exploration of similar phenomena in other nanometric two phase magnetic systems.

## Acknowledgments

This work was partially supported by the Spanish CICYT-MAT2008-06542-C04 grant. Work at Argonne is supported by the US Department of Energy, Office of Science, under contract No DEAC-02-06CH11357. M A Laguna-Marco, J Alonso and R Boada acknowledge the Ministerio de Ciencia y Tecnología of Spain for Postdoctoral and PhD grants. We would like to thank Dr Matt Ruffoni for technical assistance. SGIker technical support (MEC, GV/EJ, European Social Fund) is gratefully acknowledged.

## References

- [1] O'Handley R C 2000 *Modern Magnetic Materials: Principles and Applications* (New York: Wiley)
- [2] Nalwa H S 2000 *Magnetic Nanostructures* (Valencia, CA: American Scientific)
- [3] Xiao J Q, Jiang J S and Chien C L 1992 *Phys. Rev. Lett.* **68** 3749
- [4] Wang J Q and Xiao G 1994 *Phys. Rev. B* **49** 3982
- [5] Garitaonandia J S, Gorria P, Fernández Barquín L and Barandiarán J M 2000 *Phys. Rev. B* **61** 6150
- [6] Arcas J, Hernando A, Barandiarán J M, Prados C, Vázquez M, Marín P and Neuweiler A 1998 *Phys. Rev. B* **58** 5193
- [7] Fdez-Gubieda M L, García Prieto A, García-Arribas A, Meneghini C and Mobilio S 2002 *Europhys. Lett.* **59** 855
- [8] García Prieto A, Fdez-Gubieda M L, Meneghini C, García-Arribas A and Mobilio S 2003 *Phys. Rev. B* **67** 224415
- [9] Sarmiento G, García Prieto A and Fdez-Gubieda M L 2004 *J. Magn. Magn. Mater.* **290/291** 1071
- [10] García Prieto A, Fdez-Gubieda M L, Chaboy J, Laguna-Marco M A, Muro T and Nakamura T 2005 *Phys. Rev. B* **72** 212403
- [11] Binns C, Maher M J, Pankhurst Q A, Kechrakos D and Trohidou K N 2002 *Phys. Rev. B* **66** 184413
- [12] Jiménez-Villacorta F, Sánchez-Marcos J, Céspedes E, García-Hernández M and Prieto C 2010 *Phys. Rev. B* **82** 134413
- [13] Alonso J, Fdez-Gubieda M L, Barandiarán J M, Svalov A, Fernández Barquín L, Alba Venero D and Orue I 2010 *Phys. Rev. B* **82** 054406
- [14] Mydosh J A 1993 *Spin Glasses: An Experimental Introduction* (London: Taylor and Francis)
- [15] Hadjipanayis G C and Prinz G A 1991 *Science and Technology of Nanostructured Magnetic Materials* (New York: Plenum)
- [16] Dormann J L and Fiorani D 1992 *Magnetic Properties of Fine Particles* (Amsterdam: North-Holland)
- [17] Gregg J F, Thompson S M, Dawson S J, Ounadjela K, Staddon C R, Hamann J, Fermon C, Saux G and O'Grady K 1994 *Phys. Rev. B* **49** 1064
- [18] Hillenkamp M, Di Domenicantonio G and Félix Ch 2008 *Phys. Rev. B* **77** 014422
- [19] Soares J M, Machado F L A, de Araújo J H, Cabral F A O and Ginani M F 2005 *Phys. Rev. B* **72** 184405
- [20] Milner A, Korenblit I Ya and Gerber A 1999 *Phys. Rev. B* **60** 14821
- [21] Allia P, Coisson M, Spizzo F, Tiberto P and Vinai F 2006 *Phys. Rev. B* **73** 054409
- [22] Fähler S, Weisheit M, Kahl S, Sturm K and Krebs H U 1999 *Appl. Phys. A* **69** S459
- [23] Luo Y and Krebs H U 1995 *J. Appl. Phys.* **77** 1482
- [24] Harper J M E, Rodbell K P, Colgan E G and Hammond R H 1997 *J. Appl. Phys.* **82** 4319
- [25] Nalwa H S 2002 *Handbook of Thin Film Materials* (New York: Academic)
- [26] Liu F 2005 *Mater. Lett.* **59** 1458
- [27] Störmer M and Krebs H U 1995 *J. Appl. Phys.* **78** 7080
- [28] Abramoff M D, Magelhaes P J and Ram S J 2004 *Biophys. Int.* **11** 36
- [29] Kataoka N, Sumiyama K and Nakamura Y 1985 *J. Phys. F: Met. Phys.* **15** 1405
- [30] Li Z G, Wan H, Liu J, Tsoukatos A, Hadjipanayis G C and Liang L 1993 *Appl. Phys. Lett.* **63** 3011
- [31] Koningsberger D C and Prins R 1988 *X-ray Absorption: Principles, Applications, Techniques of EXAFS, SEXAFS and XANES* (New York: Wiley-Interscience)
- [32] Ankudinov A L, Nesvizhskii A I and Rehr J J 2003 *Phys. Rev. B* **67** 115120
- [33] Eisenberg P and Brown G S 1979 *Solid State Commun.* **29** 481
- [34] De Crescenzi M, Balzarotti A, Comin F, Incoccia L, Mobilio S and Motta N 1981 *Solid State Commun.* **37** 921
- [35] Fdez-Gubieda M L, Orue I, Plazaola F and Barandiarán J M 1996 *Phys. Rev. B* **53** 620
- [36] Fdez-Gubieda M L, García-Arribas A, Orue I, Plazaola F and Barandiarán J M 1997 *Europhys. Lett.* **40** 43
- [37] García-Arribas A, Fdez-Gubieda M L and Barandiarán J M 2000 *Phys. Rev. B* **61** 6238
- [38] Fdez-Gubieda M L, García-Arribas A, López Antón R, Orue I, Gorria P, Pizzini S and Fontaine A 2000 *Phys. Rev. B* **62** 5746
- [39] Sasaki M, Jönsson P E, Takayama H and Mamiya H 2005 *Phys. Rev. B* **71** 104405
- [40] Fernández Barquín L, Gómez Sal J C, Gorria P, Garitaonandia J S and Barandiarán J M 2003 *J. Non-Cryst. Solids* **329** 94
- [41] Haetinger C M, Ghivelder L, Schaf J and Pureur P 2009 *J. Phys.: Condens. Matter.* **21** 506006
- [42] Barandiarán J M, Gorria P, Orue I, Fdez-Gubieda M L, Plazaola F, Gómez Sal J C, Fernández Barquín L and Fournes L 1997 *J. Phys.: Condens. Matter* **9** 5671
- [43] Hernando A, Marín P, Vázquez M, Barandiarán J M and Herzer G 1998 *Phys. Rev. B* **58** 366
- [44] Chien C L and Unruh K M 1983 *Phys. Rev. B* **28** 1214
- [45] Nogués J and Schuller I K 1999 *J. Magn. Magn. Mater.* **192** 203
- [46] Yuan F T, Lin J K, Yao Y D and Lee S F 2010 *Appl. Phys. Lett.* **96** 162502
- [47] Morita H, Hiroyoshi H and Fukamichi K 1986 *J. Phys. F: Met. Phys.* **16** 507
- [48] Sort J, Langlais V, Doppio S, Dieny B, Suriñach S, Muñoz J S, Baró M D, Laurent Ch and Nogués J 2004 *Nanotechnology* **15** S211
- [49] Chaboy J, Laguna-Marco M A, Sánchez M C, Maruyama H, Kawamura N and Suzuki M 2004 *Phys. Rev. B* **69** 134421
- [50] Laguna-Marco M A, Piquer C and Chaboy J 2009 *Phys. Rev. B* **80** 144419
- [51] Jaouen N, Wilhelm F, Rogalev A, Goulon J, Ortega L, Tonnerre J M and Yaresko A 2008 *J. Phys.: Condens. Matter* **20** 095005
- [52] Xu Y B, Zhai H R, Lu M, Jin Q Y and Miao Y Z 1992 *Phys. Lett. A* **168** 213
- [53] Vogel J, Fontaine A, Cros V, Petroff F, Kappler J P, Krill G, Rogalev A and Goulon J 1997 *Phys. Rev. B* **55** 3663
- [54] Chaboy J, Bartolomé F, Ibarra M R, Marquina C I, Algarabel P A, Rogalev A and Neumann C 1999 *Phys. Rev. B* **59** 3306
- [55] Hashizume H, Ishiji K, Lang J C, Haskel D, Srajer G, Minár J and Ebert H 2006 *Phys. Rev. B* **73** 224416
- [56] Bartolomé J et al 2008 *Phys. Rev. B* **77** 184420
- [57] Tyer R, van der Laan G, Temmerman W M, Szotek Z and Ebert H 2003 *Phys. Rev. B* **67** 104409